Materials Research Express

PAPER

The behavior of hydrothermally synthesized hematite nanorods prepared on spin coated seed layers

Joan Talibawo[1,2], Justine S Nyarige[2], Pannan I Kyesmen[2], Marie C Cyulinyana[1] and Mmantsae Diale[2]

[1] African Center of Excellence in Energy and Sustainable Development, University of Rwanda, PO Box 3900 KN 67 Street Nyarugenge, Kigali, Rwanda
[2] Department of Physics, University of Pretoria, Private Bag X20, Hatfield 0028, South Africa

E-mail: mmantsae.diale@up.ac.za

Keywords: hematite, nanorods, hydrogen, photoelectrochemical water splitting

OPEN ACCESS

RECEIVED
19 November 2021

REVISED
3 January 2022

ACCEPTED FOR PUBLICATION
12 January 2022

PUBLISHED
8 February 2022

Abstract

Herein we report on the effect of varied spin-coated seed layer concentrations of Iron (III) chloride hexahydrate ($FeCl_3.6H_2O$) on the photoelectrochemical performance of hydrothermally synthesized hematite nanorods. The seed layers were prepared from 0.05, 0.07, 0.09, 0.11, and 0.13 M concentrations of $FeCl_3.6H_2O$. The nanorods were vertically aligned with slight inclinations over the seed layers with the two lowest molar concentrations (0.05 and 0.07 M) of $FeCl_3.6H_2O$. A further increase in seed layer concentrations transformed the nanorods as they grew over others and agglomerated into clusters. Structural analysis using x-ray diffraction (XRD) and Raman spectroscopy demonstrated uniform hematite crystalline peaks for all the samples. All samples absorbed highly in the visible region within an onset absorption edge wavelength ranging from 624 to 675 nm. Overall, the nanorods synthesized over the lowest seed layer concentration of 0.05 M of $FeCl_3.6H_2O$ exhibited the highest photocurrent density of 0.077 mA cm^{-2} at 1.5 V versus reversible hydrogen electrode. The results obtained provide important information about the structural, optical, and photoelectrochemical properties of hematite nanorods synthesized over varied seed layer concentrations. This is a key contribution in understanding and enhancing the hematite nanorods performance for photocatalytic applications.

1. Introduction

Photoelectrochemical (PEC) water splitting is one of the methods of converting solar energy to chemical energy in the form of hydrogen [1, 2]. The process involves irradiation of the active electrode in an aqueous electrolyte. The photoinduced reactions that follow activate oxidation of water at the electrode-electrolyte interface and reduction at the counter electrode, hence producing oxygen and hydrogen respectively [3]. A major challenge facing this technology is the availability of an efficient photoelectrode to produce the required efficiency for device application. Over the years, many metal oxide semiconductors like Cuprous oxide (Cu_2O) [4], titanium dioxide (TiO_2) [5], tungsten oxide (WO_2) [6], and hematite (α-Fe_2O_3) [7] have been investigated for their suitability in PEC applications. Among these, hematite, an n-type semiconductor, has been reported to be highly promising due to its stability in a wide pH range, earth-abundance, and a valence band edge positioning that is thermodynamically fitting for oxygen evolution [8, 9]. Furthermore, hematite has a narrow bandgap that ranges from 1.9 to 2.2 eV which can absorb up to 40% of the visible light and achieve a maximum theoretical solar-to-hydrogen (STH) conversion efficiency of 16.8% at a bandgap of ~2.0 eV [7, 10]. However, this efficiency is yet to be realized at low bias, due to poor conductivity of hematite and small hole diffusion lengths (~2–20 nm) through the semiconductor-electrolyte interface [11]. Besides, the excitation lifetime for hematite is very small (~10 ps) [5]. These shortcomings lead to fast electron-hole recombination, ultimately affecting the hematite PEC water oxidation potential [12]. However, studies have proved that nanostructured hematite such as nanoparticles [13], nanosheets [14], nanospheres [15], cauliflowers [16], and nanorods (NRs) [17], show improved performance in PEC applications. The use of these nanostructures minimizes losses due to charge

recombination in the semiconductor bulk by scaling down the diffusion depth of holes across the semiconductor material [7, 18]. Additionally, nanostructured hematite increases the surface area for photon absorption [19]. In this context, hematite NRs have been widely studied as photoanodes for PEC water splitting [20].

While nano-engineering of electrodes addresses some of the limiting factors for hematite performance, a multifaceted approach to address the various limitations of material performance is reported to yield better results [21]. For example, a study conducted by Sun *et al* used a consolidated strategy of doping, surface-etching, and seed layering to enhance the performance of hematite NRs [18]. In another study, Jiang *et al* synthesized hematite NRs over a TiO_2 seed layer and further modified the surface with TiO_2 treatment, and the results gave an increased photocurrent density of 1.49 mA cm^{-2} from 0.005 mA cm^{-2} at 1.23 V versus RHE of the bare NRs [22]. The use of seed layers is reported to enhance the redox reactions at the photoelectrodes by cutting down on the electron back-injection at fluorine-doped tin oxide (FTO) coated glass substrate-electrolyte interface [18]. Similarly, it hampers the electron-hole recombination between the FTO and the semiconductor [23]. In addition, seed layers under specific temperature conditions induce dopants into the semiconductor electrode, subsequently influencing its electrical properties [24]. To this effect, Ludmilla and co-workers tripled donor densities of ultrathin (10–15 nm) hematite films to 2×10^{20} cm^{-3} by growing them over Nb_2O_5 and SiO_2 seed layers [23] . Sun and co-workers also demonstrated a 110 mV cathodic shift of onset potential for hematite NRs grown on SnO_2/SiOx, and α-Fe_2O_3:Ti under layers [18]. However, the dynamic influence of hematite seed layering on the structural, optical, and PEC performance of hematite NRs has not been reported.

In this work, we report the influence of spin-coated seed layers on the structural, morphological, optical properties, and PEC performance of hematite NRs. The seed layers were prepared using varied $FeCl_3.6H_2O$ precursor concentrations. Thereafter, NRs were prepared over the seed layers using the conventional energy-saving hydrothermal technique. Results indicate that the nanorod arrays synthesized over the seed layer with the lowest precursor concentration produced the highest photocurrent density of 0.077 mA cm^{-2} at 1.5 V versus RHE. Notably, these results correlate well with the high donor density of the charge carriers, and the overall thin hematite layer (337.7 nm) over the FTO substrate.

2. Experimental procedure

2.1. Materials and substrate preparation

$FeCl_3.6H_2O$, 97% and sodium nitrate ($NaNO_3$, 98%) were obtained from Sigma Aldrich and used as received. Fluorine doped tin oxide (FTO) substrates were ultrasonically cleaned in ten-minute intervals using sodium stearate ($C_{18}H_{35}NaO_2$) soap solution, ethanol, and acetone. The substrates were rinsed with deionized water after each step. The cleaned FTO substrates were then dried using flowing nitrogen gas.

2.2. Synthesis of seed layers

Hematite seed layers were synthesized on FTO substrates using the spin coating method as illustrated in figure 1(a). The spin-coated layers were prepared from solutions of 0.05, 0.07, 0.09, 0.11, and 0.13 M concentrations of $FeCl_3.6H_2O$ using methanol as solvent. The solution was dropped on the substrate and spin-coated at 3000 rpm for 30 s. The process was repeated fifteen times, to grow the desired thickness of the seed layers, with alternate intervals of drying time in the oven at 30 °C. Thereafter, the seed layers were annealed in air at 500 °C for 1 h and left to cool to room temperature and used for the growth of the NRs.

2.3. Synthesis of hematite NRs

Before growing the hematite NRs, FTO substrates nucleated with hematite seed layers were first covered at the back (non-conducting side) and a little section of the conducting side using Kapton tape and then carefully placed at the bottom of the Teflon container, with the seeded layers facing upwards. A 90 ml Teflon container was partially filled with a 45 ml aqueous solution of thoroughly mixed 0.15 M $FeCl_3{\cdot}6H_2O$ and 1 M $NaNO_3$, based on previous works by Hemin Zhang and co-workers [21]. The container was placed in a stainless-steel reactor, tightly closed, and then placed in the oven as shown in figure 1(b). The NRs were hydrothermally grown over the hematite seed layers in a laboratory oven at 100 °C for 8 h (h) including the ramping time. After this time-lapse, the oven was turned off and the autoclave was left to cool to room temperature. Yellowish layers of iron (III) oxyhydrate (FeOOH) were formed on the substrates. The samples were washed thoroughly with deionized water to get rid of extra iron salts, dried out in open air, and finally annealed through the same conditions as the seed layers. Samples were marked based on the technique used to synthesize the seed layer and precursor concentrations: spin coated samples SC1 (0.05 M), SC2 (0.07 M), SC3 (0.09 M), SC4 (0.11 M), and SC5 (0.13 M) as shown in figure 1.

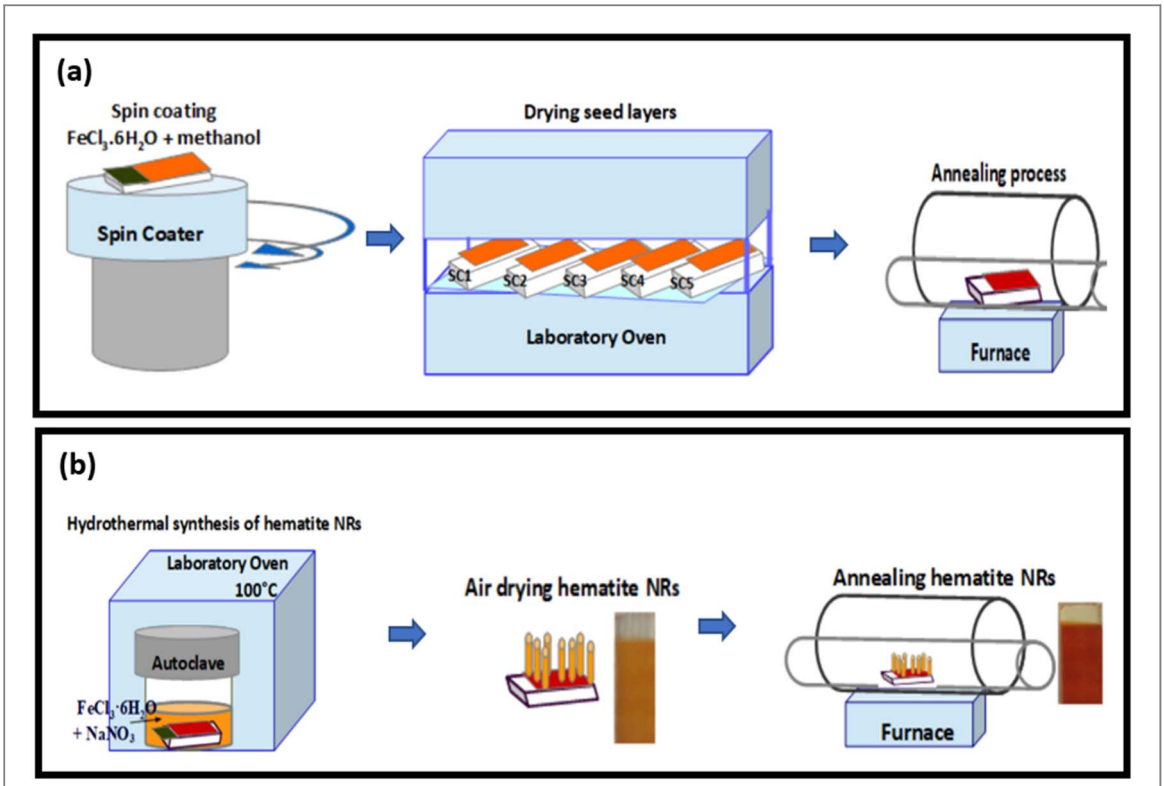

Figure 1. Schematic illustration of (a) the synthesis of hematite seed layers over FTO substrates using 0.05, 0.07, 0.09, 0.11, and 0.13 M concentrations of $FeCl_3.6H_2O$ and (b) the synthesis of hematite NRs over all the spin-coated FTO/hematite seed layers in (a).

2.4. Characterization

Analysis of the surface morphology of the seed layers and the NRs were done using Zeiss Ultra PLUS field emission scanning electron microscope (FE-SEM) set at 1 kV. The cross-sectional FE-GEM views of the samples were obtained to estimate the thicknesses of the seed layers. Structural analysis of the NRs was performed using Bruker D2 Phaser x-ray diffractometer, with CuK_{α} radiation. The vibrational modes of hematite were obtained using a WITec alpha 300 RAS + confocal micro-Raman microscope (Focus Innovations, Germany) with a 532 nm green laser over a 150 s spectral acquisition time and laser power of 3 mW. Absorption measurements of hematite NRs were performed using an Agilent Cary-60 Ultraviolet-Visible (UV–vis) spectrophotometer at wavelengths ranging from 200–800 nm.

A three-electrode electrochemical setup in a Teflon container, connected to a VersaSTAT 3F potentiostat from Princeton Applied Research workstation equipment was used for the PEC analysis of the hematite NRs. The samples acted as the working electrodes (WE) alongside a 2 × 2 cm platinum mesh counter electrode (CE), and an Ag/AgCl in 3M KCl reference electrode (RE) within a 1 M NaOH (pH of 13.6) aqueous solution electrolyte. An area of approximately (0.7 × 0.7) cm [2] of the photoanode was irradiated by the solar simulator (1 sun at 100 mW cm^{-2} Newport 91150V lamp). A scan rate of 0.05 V s^{-1} was used to obtain linear sweep voltammetry (LSV) measurements within a voltage ranged of −0.9 to 0.8 V with and without the illumination of the photoanode samples. The potential values obtained were then converted to RHE using the Nernst equation (equation (1)) [15].

$$E_{RHE} = E_{Ag/AgCl} + (0.059pH) + E_{Ag/AgCl} \quad (1)$$

where E_{RHE} is the RHE potential, $E_{Ag/AgCl}$ is the potential, and $E_{Ag/AgCl} = 0.205\ V$ derived from experimental results at 25 °C versus the Ag/AgCl reference electrode in the PEC cell set up. The Mott-Schottky measurements were done at a DC potential span ranging from 1.2 to 0.5 V versus Ag/AgCl, in the dark, at a frequency of 10 kHz, and an AC peak potential of 10 mV. All PEC measurements were done under the illumination of the conducting sides of the photoanodes.

3. Results and discussion

3.1. Surface morphology and thickness of seed layers

The SEM images of the SC1, SC2, SC3, SC4 and SC5 spin coated hematite seed layers are shown in figure 2. The surface images of the samples showed compact and agglomerated crystal grains of hematite nanoparticles. Based

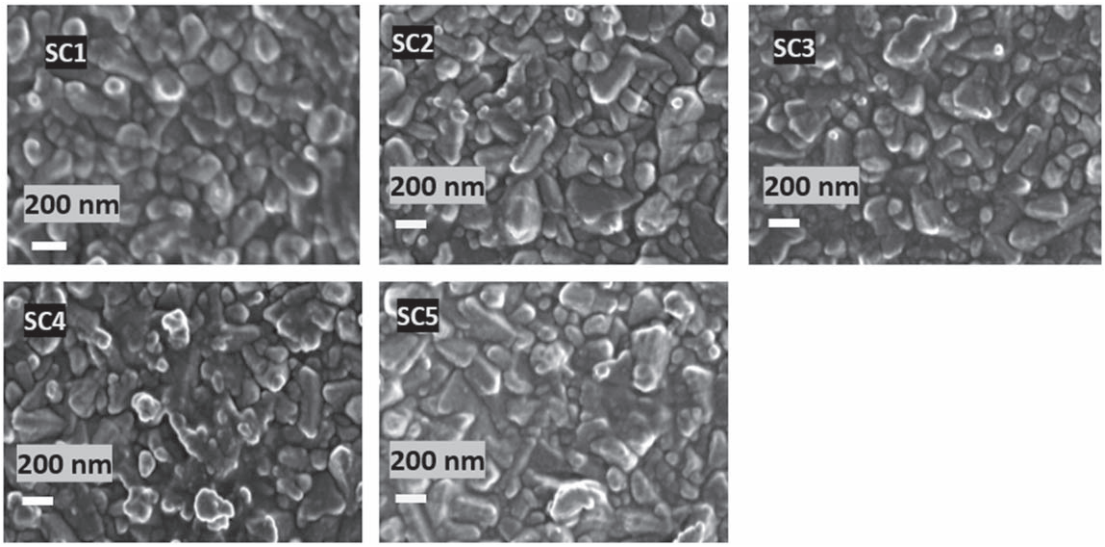

Figure 2. SEM images of SC1, SC2, SC3, SC4, and SC seed layers spin coated from 0.05, 0.07, 0.09, 0.11, and 0.13 M precursor concentrations of $FeCl_3.6H_2O$.

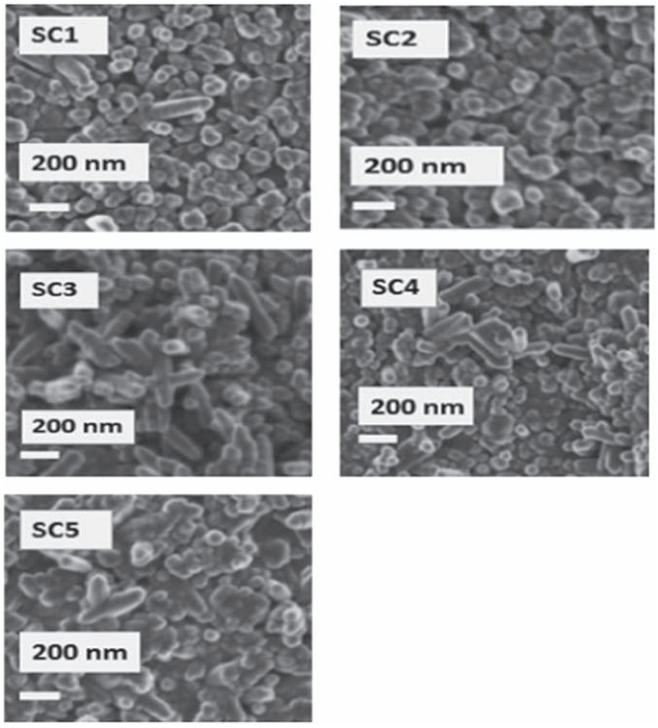

Figure 3. SEM images for α-Fe_2O_3 NRs synthesized over different seed layers prepared by spin coating method using 0.05, 0.07, 0.09, 0.11, and 0.13 precursor concentrations of $FeCl_3.6H_2O$ presented as SC1, SC2, SC3, SC4, and SC5 respectively.

on the morphology of the samples, the compact grains appeared to be more agglomerated with increasing precursor concentration.

Figure 3 shows surface morphologies of hematite NRs labelled SC1, SC2, SC3, SC4, and SC5, respectively. Vertically aligned NRs were revealed and appeared quite distinct though closely packed for samples with seed layers of 0.05 (SC1) and 0.07 M (SC2) concentrations. A further increase in seed layer concentration for the SC3 sample exhibited dispersed nanorod arrays. The SC4 sample NRs started to coalesce and stack up over each other, causing secondary nucleation sites for other NRs to grow. The NRs coalesced further into clusters with an increase in concentration as observed with the SC5 sample. The hematite NRs became less distinct and vertically aligned with increasing seed layer concentration. This was likely due to the increased agglomeration of nanoparticles in the seed layers, leading to a reduction in surface area for growth of the hematite NRs. This

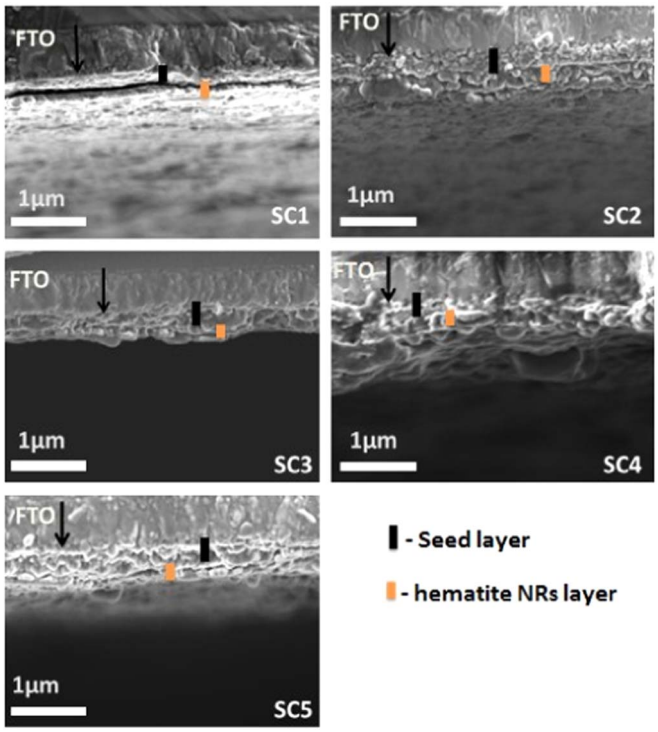

Figure 4. Cross-sectional SEM views of the seeded hematite NRs, and estimations of the seed layer thicknesses over the FTO substrates for samples SC1, SC2, SC3, SC4, and SC5.

Table 1. Estimations of the seed layer, and total film thickness of the samples.

NRs Samples	Seed layer thickness (nm)	NRs thickness (nm)	Total film thickness (nm)
SC1	155.2	182.5	337.7
SC2	204.5	382.0	586.5
SC3	237.0	137.9	374.9
SC4	250.1	228.0	478.1
SC5	301.3	146.1	447.4

observation conforms with other literature where morphological adjustments for hematite NRs was influenced by the morphology of the seed layers [24].

The cross-sectional morphology of the seeded hematite NRs samples shown in figure 4 was used to analyze the seed layer thicknesses across the samples with varied precursor concentrations. We observed an increase in seed layer thicknesses ranging from 155.2 to 301.3 nm as the precursor concentration increased as shown in table 1. Furthermore, the precursor concentrations were noted to directly impact the seed layer thicknesses. The thicknesses of the seed layers and the nanorods were added (figure 5) to study the effect on the absorption and the photocurrent response of the films. The total thickness of the NRs and seed layer films was 337.7, 586.5, 374.9, 478.1, and 447.4 nm for SC1, SC2, SC3, SC4, and SC5, respectively. Notably, hematite films within a 400–500 nm thickness range have been observed to effectively absorb light for PEC applications due to its low absorption coefficient that weakly starts around the near infrared region and suddenly increases in the visible spectral region[25]. To this effect, the recorded overall thicknesses across different samples are around the suitable range for effective light absorption. SC2 sample presented the largest overall thickness. We attributed this to two main reasons. First, the vertically aligned NRs exhibited by the SC2 samples contribute to its large film thickness. Also, their seed layer thickness was relatively higher than the SC1 samples. However, more investigations still need to be done for a better understanding of the high film thickness exhibited by SC2 samples relative to others.

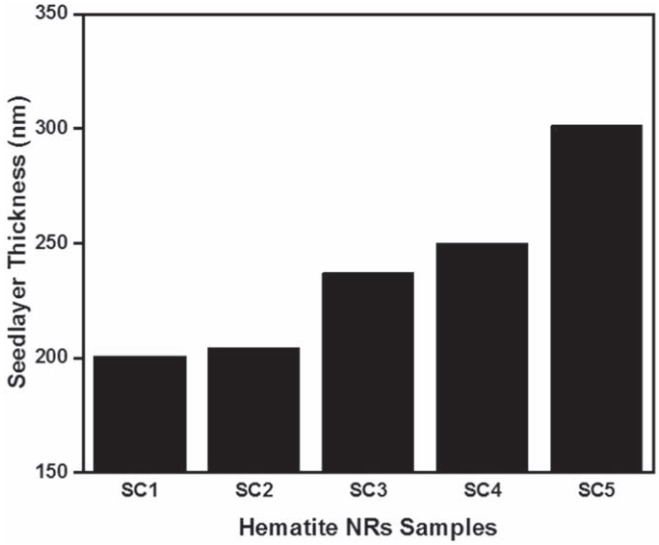

Figure 5. Bar graph showing the varied seed layer thicknesses across the samples.

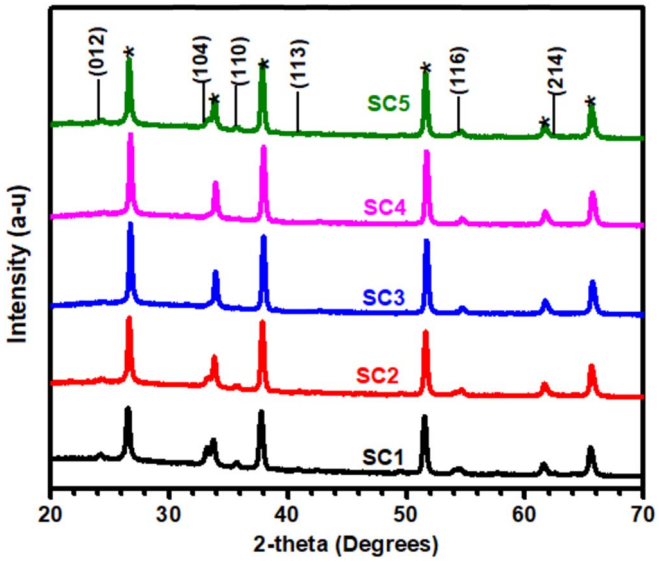

Figure 6. X-Ray diffraction spectra of spin-coated hematite seed layers prepared using precursor concentrations of 0.05, 0.07, 0.09, 0.11, and 0.13 M of $FeCl_3.6H_2O$. The symbol * shows the peaks of SnO_2 originating from FTO substrate.

3.2. Structural analysis

Figure 6 presents the XRD pattern of the spin coated hematite seed layers. The main diffraction peaks of hematite were observed at (104), (110), (116), and (214) planes and are indexed at 33.1°, 35.6°, 54.0°, and 62.4°, respectively. The peaks are associated with hematite according to JCPDS file no. 33–0664 for α-Fe_2O_3 [26]. These peaks confirm a uniform crystalline phase structure and the purity of the hematite seed layers. The SnO_2 peaks from the FTO substrate associated with the JCPDS card # 41–1445 were also present and indexed at 26.6, 33.9, 38.5, 51.8, 62.6, and 65.9°, respectively [27]. They are indicated by the asterisk sign on the diffraction pattern.

The average crystallite size (D) for the hematite seed layers was calculated using the Debye–Scherrer's expression (equation (2)) [28].

$$D = K\lambda/\beta \cos\theta \tag{2}$$

where K is the Scherrer constant (0.9), λ is the wavelength of the CuK_α radiation (0.15418 nm), β is the full-width at half-maximum (FWHM) of the preferential diffraction peak, and θ the Bragg angle. The three dominant hematite peaks at 35.6°, 54.0°, 62.4°were used in the analysis of crystallite size. The average crystal sizes for the hematite seed layers were 9.5, 10.7, 11.1, 15.8, and 18.2 nm for SC1, SC2, SC3, SC4, and SC4 samples

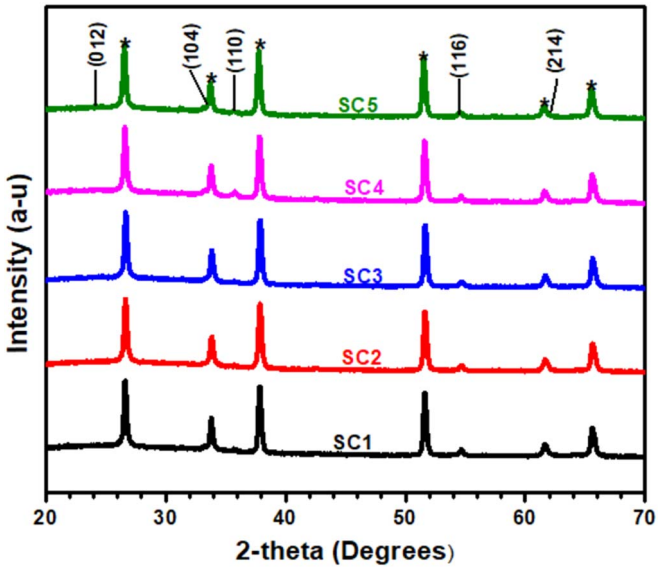

Figure 7. X-ray diffraction spectra of hematite NRs arrays synthesized over spin-coated hematite seed layers. The symbol * shows the peaks of SnO_2 originating from FTO substrate.

respectively. The crystal sizes were confirmed to increase with increasing precursor concentration. The smaller the crystal sizes, the more the surface area that will be available for the growth of hematite NRs. The smaller particle sizes obtained for the seed layers of samples SC1 and SC2 provided large surface area which may have supported the growth of the more vertically align NRs observed for the films compared to others (figure 3).

Figure 7 presents XRD patterns for the seeded hematite NRs films annealed at 500 °C for 1 h. The peaks were indexed in their respective 2-theta angles and confirmed with the JCPDS file no. 33–0664 for α-Fe_2O_3 [26]. All samples correspond to a rhombohedral hematite structure with key peak presentations of (104), (110), (116), and (214) indexed at 33.1°, 35.6°, 54.0°, and 62.4° respectively. This reflects a common crystalline phase for the hematite NRs samples. The absence of extra peaks within the 50° to 70° 2-theta angle range further confirms the purity of the hematite NRs. Studies have shown that photo-enhanced charge flow in hematite is reported to be dominant in the (110) plane [29, 30]. In this study, the preferential growth in the (110) plane is more exhibited by SC1 and SC4 samples relative to the other films and can influence their photocatalytic properties. The low preferential growth in the (110) plane generally observed for the samples is attributed to the low annealing temperature of 500 °C which deterred the samples' crystallinity [31]: an enhancement factor for charge transport in hematite photocatalysis [29]. Intense SnO_2 peaks from the FTO substrate were also observed for (110), (111), (211), and (301) at 26.6, 38.5, 51.8°, and 65.9° respectively indexed according to JCPDS 41–1445 [32]. The average crystallite size (D) for the as-prepared hematite NRs was also calculated using the Debye–Scherrer's expression (equation (2)).

The average crystallite size values obtained were ~8.3, 8.2, 8.2, 8.3, and 8.3 nm for SC1, SC2, SC3, SC4, and SC5, respectively. This result indicates that the varied seed layer concentrations had no significant effect on the crystallite sizes of the hematite NRs. The similar crystallite sizes obtained for the samples might be attributed to the uniform precursor concentration and annealing temperature used for the growth of the NRs. The precursor concentration and annealing temperature are reported to impact the crystallite sizes of hematite films [28].

Raman spectroscopy measurements confirmed the structural properties obtained from the XRD results of the seeded hematite NRs samples. From the Raman analysis, seven uniform lattice vibrational modes associated with hematite were observed across all samples as shown in figure 8. The modes were well-matched with the hematite active phonon modes E_g for peaks at 247, 293, 299, 412, and 613 cm^{-1}, whereas peaks at 225 and 490 cm^{-1} were assigned to the A_{1g} mode. The longitudinal optical (LO) and 2LO peaks at 656 cm^{-1} and 1313 cm^{-1} reveal the ferromagnetic nature of hematite [15, 33]. The Raman studies indicate that the hematite phase remained the same through the hydrothermal process which agrees with the XRD analysis. The intensities of the layered samples are comparably significant and increases with increasing seed layer concentrations. This is correlated with the increasing overall film thickness of the samples since the Raman intensity increases with the surface density of the material that interacts with the light [34, 35]. Similarly, the less compact and randomly dispersed NRs presented by the SC3 sample may have resulted in the decreased Raman intensity observed for the film.

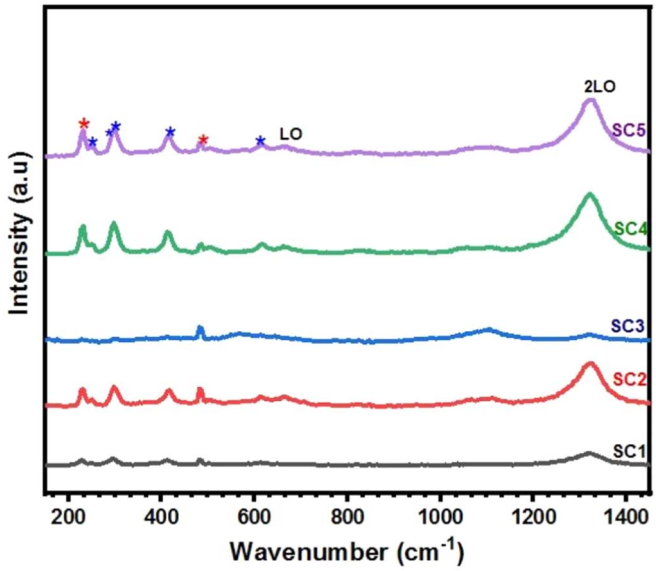

Figure 8. Raman spectra of the A_{1g} and E_g vibrational modes of hematite NRs prepared over varied seed layer precursor concentrations of $FeCl_3.6H_2O$.

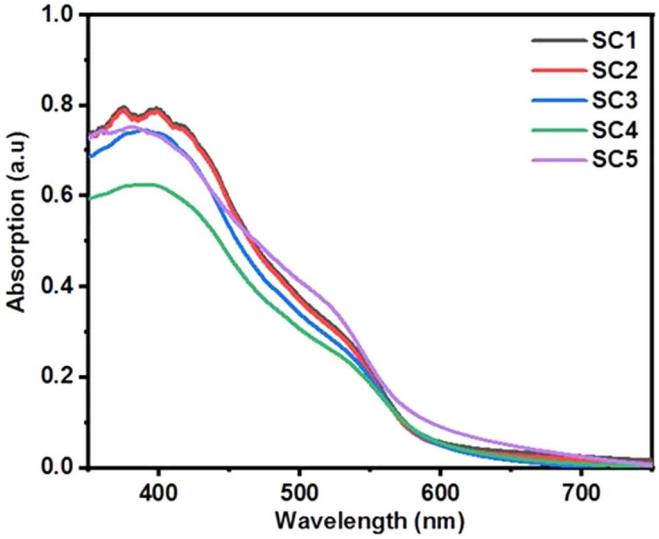

Figure 9. The absorbance of hematite NRs grown on seed layers with varied precursor concentrations.

3.3. Optical properties

The absorption properties of the hematite NRs prepared on seed layers from different precursor concentrations were analyzed based on results in figure 9. All the hematite NRs films absorbed highly in the visible region. However, the absorption gradually decreased as the wavelength increases and flattened out beyond 600 nm in conformity with reported literature [15, 36]. This syncs further with featured observations of hematite nanostructures noted to absorb more at wavelengths less than the red line absorption edge of ~647 nm [26, 37]. The onset photo absorption wavelength ranged from 624 to 675 nm for all samples with SC1 and SC2 having comparably higher values. The thickness of the SC2 sample as shown in table 1 obtained from figure 4 is higher than that of SC1, indicating an increase in photon penetration distance towards the back contact of the FTO substrate. According to Beer–Lambert's law, film absorbance improves with gain in film thickness [38, 39]. Equation (3) shows the Beer–Lambert relation to this analysis.

$$A = \varepsilon bc \tag{3}$$

where A is the absorbance, ε is the absorbency index (0.4343α), b is the length of the path taken by the photons in the absorbing material, and c is the concentration of the absorber material [40, 41]. Considering the limiting hole diffusion length of hematite, the photogenerated electron-hole pairs in the bulk of the films will likely

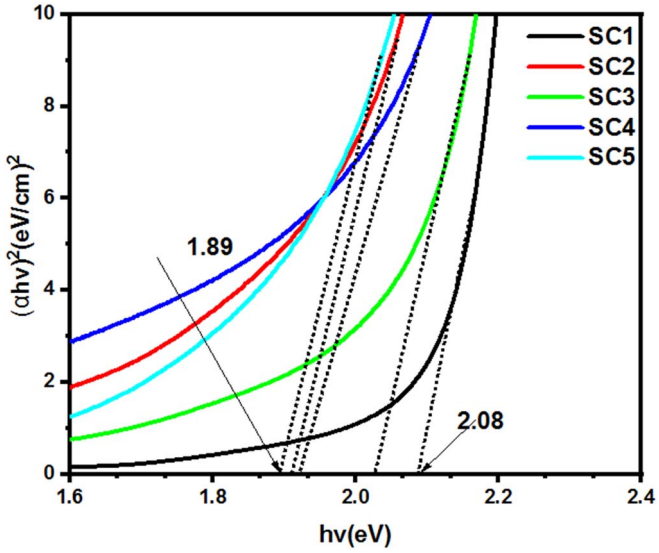

Figure 10. Tauc plots for seeded hematite NRs samples arrays grown on seed layers with varied precursor concentrations.

recombine before getting to the hematite-electrolyte interface, consequently affecting the photocurrent produced. Therefore, whilst the sample absorption is high, the small hole diffusion depth of hematite is anticipated to affect photocurrent generation by the photoanode. Similarly, SC5 and SC3 samples followed in line with absorption levels due to their overall thicknesses, in comparison to SC1. SC4 presented the lowest absorption despite recording the second-highest overall thickness. The surface morphology of the hematite NRs likely influenced the photon absorption properties. The random orientations of the secondary NRs observed over the coalesced NRs may have limited light scattering and likely enhanced surface reflection by the SC4 samples, resulting in the low photon absorption observed for the films. Sample SC1 that had the least overall thickness equally recorded a high absorbance due to enhanced light scattering and reflection presented by the wide surface area of the vertically aligned NRs [42]. The coalesced and overlapping NRs in SC3, SC4, and SC5 could also have limited the incident light scattering and multiple reflections reported to enhance absorption [27, 43]. This result shows that the hematite NRs absorption can be tuned by controlling the seed layer thickness. The seed layers prepared with lower precursor concentration provided larger surface area for NRs growth and resulted in more vertically align NRs which enhanced photon scattering and absorption.

The indirect bandgap values for the samples were estimated using fitted Tauc plots of $(\alpha hv)^2$ versus hv derived from the Tauc expression in equation (4) [44].

$$\alpha hv = A(hv - E_g)^n \tag{4}$$

where α denotes the absorption coefficient, h is the planks constant, v is the frequency of light, A represents a constant derived from the effective mass of the electrons and holes, E_g is the bandgap, and prefix n is 0.5 or 2 for the direct and indirect band gaps transitions, respectively. The direct transitions are associated with the $O^{2-}2p \rightarrow Fe^{3+}$ charge shift whereas the indirect transitions represent the spin-forbidden Fe^{3+} $3d^{-3}$ 3d excitation [45]. Tangents of the plots were extrapolated to obtain the hv-axis intercepts for the bandgap values as shown in figure 10. The bandgap values ranged from 1.89 to 2.08 eV and are closely comparable to reported values worked out from absorbance and Tauc plots of hematite films [15, 29].

3.4. Current-voltage measurements

A linear sweep voltammetry scan was performed for all the hematite NRs samples in the dark and under illumination to study their photocurrent yields and onset potential. All samples irrespective of the variation in seed layer concentrations yielded some photocurrents as well as dark currents as shown in figure 11. The current that flows, is majorly dependent on the bulk and interfacial reactions between the electrolyte and the NRs arrays when illuminated, and the charge transport from the semiconductor to the FTO substrate. Results of the photocurrent densities generated from the hematite NRs at 1.45 and 1.50 V versus RHE are presented in table 2. SC1 with the lowest seed layer concentrations of 0.05 M, exhibits the highest photocurrent densities of 0.03 mA cm^{-2} and 0.077 mA cm^{-2} at 1.45 V and 1.5V versus RHE respectively. The highest photocurrent for SC1 could be linked to the small overall thickness of the hematite film and preferential growth in the (110) plane. According to Heejung *et al*, thin layers directly address limitations of the short hole diffusion length and short life span for the charge carriers in the bulk as excited electrons move to the back contact of the electrode during PEC

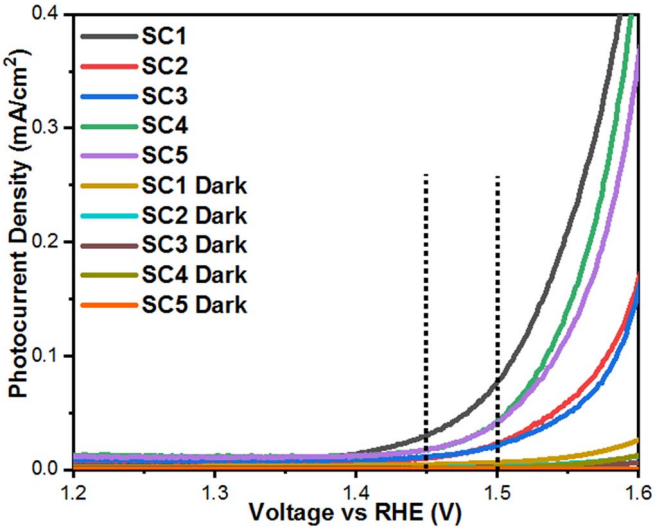

Figure 11. Voltage-Current measurements of hematite nanorods grown on spin-coated seed layers prepared with varying precursor concentrations.

Table 2. Photocurrent densities at for the seeded hematite NRs samples at 1.45 V and 1.50 V versus RHE.

NRs Samples	Photocurrent densities at 1.45 V versus RHE (mA cm^{-2})	Photocurrent densities at 1.50 V versus RHE (mA cm^{-2})
SC1	0.030	0.077
SC2	0.010	0.023
SC3	0.011	0.021
SC4	0.018	0.043
SC5	0.018	0.042

reactions [46]. In a similar context, the SC5 produced the second-highest photocurrent whereas the SC2 sample with the highest thickness of 586.5 nm presented the least photocurrent followed by SC3. More importantly, the SC1 sample that yielded the highest photocurrent, had the lowest onset potential, depictive of low surface trapping states [47]. The photocurrent densities of all samples noticeably yielded lower onset potentials compared to those of the dark currents. This is attributed to the enhanced suppressed leakage of dark currents from the electron back-injection, associated with the use of seed layers [48]. This observation compares well with the dark current onset potential range presented by seeded hematite NRs in comparison with those directly grown on FTO by Sun *et al* [18].

3.5. Mott-Schottky analysis

Mott-Schottky results of the seeded hematite NRs photoanodes were plotted as shown in figure 12. The Mott-Schottky plots were used to estimate the flat band potential (V_{fb}) and donor density (N_D) values of the hematite photoanodes based on equation (5) [29].

$$C^{-2} = \frac{2}{\varepsilon\varepsilon_0 eA^2 N_D}\left(V - V_{fb} - \frac{KT}{e}\right) \tag{5}$$

where C refers to the space charge capacitance, A is the surface area of the electrode, ε is dielectric constant for hematite (80), is the permittivity of free space 8.854×10^{-12} Fm^{-1}, e is the charge of an electron 1.602×10^{-19} C, V is the applied potential, K is the Boltzmann constant (1.38×10^{-23} JK^{-1}), N_D is the carrier charge density and T is the temperature in kelvin (298 K) [25, 26]. The linear sections of the Mott-Schottky plots were fitted and used to obtain the slopes. The values of the slopes (S) obtained were used to estimate the N_D values for different samples according to equation (6).

$$S = \frac{2}{\varepsilon\varepsilon_0 eA^2 N_D} \tag{6}$$

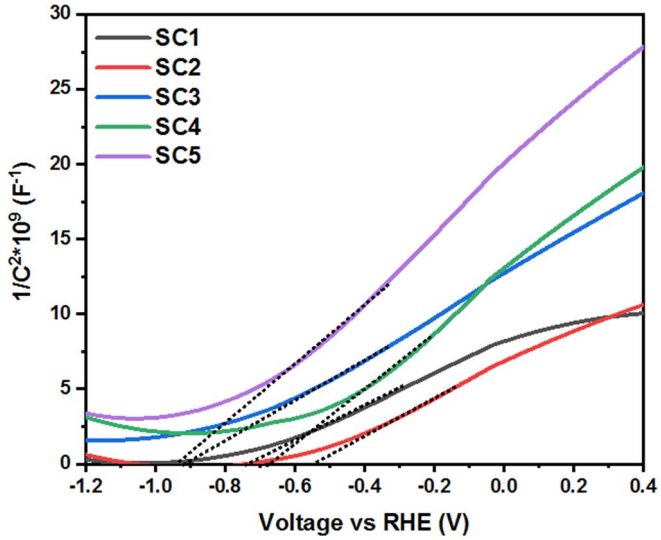

Figure 12. Mott-Schottky plots of hematite NRs grown on seed layers prepared by spin coating.

Table 3. Summary of flat band potential (V_{fb}) and donor density (N_D) values for hematite NRs grown on spin-coated seed layers of different concentrations.

NRs Samples	Total film thickness (nm)	V_{fb} versus RHE (V)	$N_D \times 10^{19}$ (cm^{-3})
SC1	337.7	0.263	5.134
SC2	586.5	0.447	4.715
SC3	374.9	0.118	3.894
SC4	478.1	0.474	2.212
SC5	447.4	0.098	2.397

The linear sections of the Mott-Schottky plots were extended to intercept the voltage (V) axis. Along this line, $\frac{1}{C^2}$ is reduced to zero and equation (4) simplifies to $V = V_{fb} + \frac{KT}{e}$ from which V_{fb} values for the samples were calculated. The approximated N_D and V_{fb} values of the seeded hematite NRs samples are shown in table 3. Positive slopes of the Mott-Schottky plots in figure 12 confirm the n-type semiconductor behavior of hematite [29].

The V_{fb} values presented by the SC1, SC2, SC3, SC4, and SC5 samples were 0.263, 0.447, 0.118, 0.474, and 0.098 V versus RHE respectively. The results depict a range of V_{fb} values for the seeded hematite NRs samples from 0.1 V − 0.5 V versus RHE, which correlates with previously reported results for hematite films [29, 49]. We observed higher V_{fb} values for SC2 and SC4 samples as shown in table 3. This is associated with the higher film thicknesses which have earlier been reported to anodically shift V_{fb} values by retarding the separation of photo-induced charges [50]. In addition, the small overall film thickness for SC1and SC3 could have enhanced the low V_{fb} values. However, we also propose that the morphological transformations of the SC3, just like SC1 could have contributed to the low V_{fb} values exhibited. According to Beermann *et al*, more vertically aligned NRs exhibited levelled flow of electrons to the back contact and fewer grain boundaries that would possibly facilitate recombination [8]. Likewise, SC5 presents the least V_{fb} value, due to its average thickness and coalesced/clustered morphology.

SC1 gives the highest N_D value of 5.134×10^{19} cm^{-3}, indicative of enhanced conductivity due to a thinner photocatalyst layer that enhances conductivity [20]. Furthermore, since hematite is characterized by short-hole diffusion length, the thin SC1 layer promotes carrier transport for the generated holes into the electrolyte [46]. Comparably, the thin layer favors the flow of the photo-generated electrons through the photoanode to the counter electrode for water reduction. Notably, high N_D values are generally linked with increased electrical conductivity according to equation (7) where δ is the conductivity, e is the electron charge, and μ is the charge mobility [39].

$$\delta = e\mu N_D \tag{7}$$

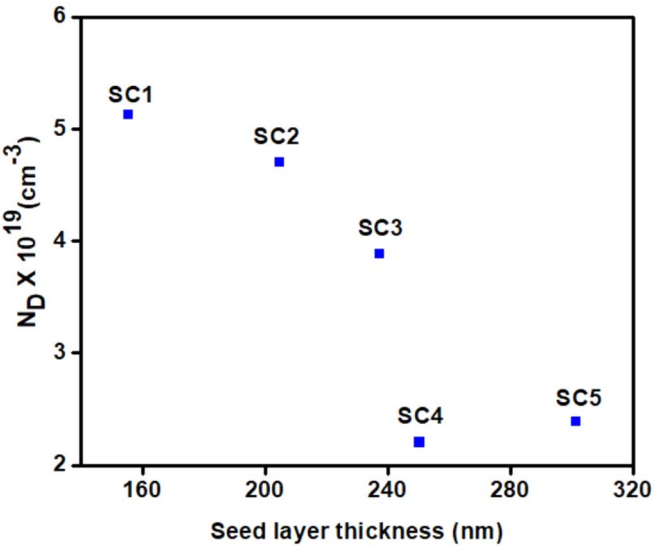

Figure 13. Seed layer thickness versus N_D values of the hematite NRs samples.

The high donor charge density in SC1 may also be linked to wide-area aspect ratio reactions through the relatively vertically aligned NRs over the seed layer compared to the morphology of other samples [8, 36]. SC3 sample presents a lower N_D of 3.894×10^{19} cm^{-3} compared to 4.715×10^{19} cm^{-3} for SC2. However, despite SC2 presenting a high N_D value, it yielded the least photocurrent. This is associated with the high overall thickness of the SC2 films. Because of the short hole diffusion length of hematite, the high thickness of SC2 films can lead to high recombination of charge carriers in the bulk of the films before they get transported to the film's surface to oxidize water [2, 11]. Also, the large thickness could have greatly increased the resistivity to the flow of electrons towards the back contact of the substrate in the SC2 sample consequently limiting the photocurrent output [51]. Our results also reveal that the N_D values of the synthesized hematite NRs decreased as the seed layer thicknesses that were tuned by the precursor concentrations, increased as shown in figure 13.

4. Conclusion

Hematite NRs were prepared over hematite seed layers synthesized by spin coating on FTO substrates. The $FeCl_3.6H_2O$ concentration of the seed layers was varied systematically by 0.02 intervals from 0.05 to 0.13 M. The overall seed layer thicknesses increased with the seed layer concentrations and affected the final morphology of the hematite NRs. The nanorod morphology at the lowest concentration presented relatively vertical NRs. As the seed layer concentration increased, the NRs became secondary nucleation sites for other NRs to grow, and later coalesced into clusters. The XRD results revealed a uniform hematite phase for all the samples. However, all the seeded hematite NRs presented low preferential growth in the more conducting plane of (110), due to the low-temperature crystallization of the samples. All samples absorbed highly in the visible region and tended to flatten out slightly beyond 600 nm. The onset absorbance for all the hematite samples ranged from 615 to 675 nm. The estimated bandgap values from our study ranged from 1.89 to 2.08 eV and agree with reported literature values for hematite films. Results also show that the smallest overall thickness of the SC1 sample of 337.7 nm, and its relative vertically aligned NRs contributed to the highest overall photocurrent density of 0.077 mA cm^{-2}.

Overall, the seed layer precursor concentrations for NRs have been confirmed to be key determinants of the seed layer thickness and influence the final overlayer morphology of the nanorods. The results in this study provide additional insight on the role of seed layer thickness in the growth of hematite NRs for photocatalytic applications.

Acknowledgments

The authors acknowledge funding and support from the African Centre of Excellence in Energy and Sustainable Development at the University of Rwanda, Department of Physics-University of Pretoria, The National Research Foundation, competitive program for rated researcher project number 118520; NRF-DST SARCHI Grant number 115463, The Organization for Women in Science for the Developing World (OWSD), and Swedish International Development Cooperation Agency (SIDA).

Data availability statement

The data generated and/or analysed during the current study are not publicly available for legal/ethical reasons but are available from the corresponding author on reasonable request.

ORCID iDs

Mmantsae Diale https://orcid.org/0000-0002-6035-6688

References

[1] Sarma S K, Mohan R and Shukla A 2020 *Mater. Sci. Semicond. Process.* **108** 104873
[2] Saremi-Yarahmadi S, Wijayantha K G U, Tahir A A and Vaidhyanathan B 2009 *J. Phys. Chem. C* **113** 4768–78
[3] Yang Y, Niu S, Han D, Liu T, Wang G and Li Y 2017 *Adv. Energy Mater.* **7** 1700555
[4] Kafi F S B, Wijesundera R P and Siripala W 2020 *physica status solidi (a)* **217** 2000330
[5] Kment S, Riboni F, Pausova S, Wang L, Wang L, Han H, Hubicka Z, Krysa J, Schmuki P and Zboril R 2017 *Chem. Soc. Rev.* **46** 3716–69
[6] Le H V, Pham P T, Le L T, Nguyen A D, Tran N Q and Tran P D 2021 *Int. J. Hydrogen Energy* **46** 22852–63
[7] Lin Y, Yuan G, Sheehan S, Zhou S and Wang D 2011 *Energy Environ. Sci.* **4** 4862–9
[8] Beermann N, Vayssieres L, Lindquist S E and Hagfeldt A 2000 *J. Electrochem. Soc.* **147** 2456
[9] Wheeler D A, Wang G, Ling Y, Li Y and Zhang J Z 2012 *Energy Environ. Sci.* **5** 6682–702
[10] Sharma P, Jang J W and Lee J S 2019 *ChemCatChem* **11** 157–79
[11] Barroso M, Pendlebury S R, Cowan A J and Durrant J R 2013 *Chem. Sci.* **4** 2724–34
[12] Zheng D, He X, Xu W and Lu X 2017 *Mater. Res. Bull.* **96** 354–9
[13] Ahmmad B, Leonard K, Islam M S, Kurawaki J, Muruganandham M, Ohkubo T and Kuroda Y 2013 *Adv. Powder Technol.* **24** 160–7
[14] Lei F, Liu H, Yu J, Tang Z, Xie J, Hao P, Cui G and Tang B 2019 *Phys. Chem. Chem. Phys.* **21** 1478–83
[15] Nyarige J S, Krüger T P and Diale M 2020 *Physica B* **581** 411924
[16] Kay A, Cesar I and Grätzel M 2006 *J. Am. Chem. Soc.* **128** 15714–21
[17] Chiam S Y, Kumar M H, Bassi P S, Seng H L, Barber J and Wong L H 2014 *ACS Appl. Mater. Interfaces* **6** 5852–9
[18] Cho I S, Han H S, Logar M, Park J and Zheng X 2016 *Adv. Energy Mater.* **6** 1501840
[19] Lindgren T, Wang H, Beermann N, Vayssieres L, Hagfeldt A and Lindquist S-E 2002 *Sol. Energy Mater. Sol. Cells* **71** 231–43
[20] Mulmudi H, Mathews N, Dou X, Xi L, Pramana S, Lam Y and Mhaisalkar S 2011 *Electrochem. Commun.* **13** 951–4
[21] Zhang H, Park J H, Byun W J, Song M H and Lee J S 2019 *Chem. Sci.* **10** 10436–44
[22] Wang J, Feng B, Su J and Guo L 2016 *ACS Appl. Mater. Interfaces* **8** 23143–50
[23] Steier L, Herraiz-Cardona I, Gimenez S, Fabregat-Santiago F, Bisquert J, Tilley S D and Grätzel M 2014 *Adv. Funct. Mater.* **24** 7681–8
[24] Milan R, Cattarin S, Comisso N, Baratto C, Kaunisto K, Tkachenko N and Concina I 2016 *Sci. Rep.* **6** 1–10
[25] Sivula K, Le Formal F and Grätzel M. 2011 *ChemSusChem* **4** 432–49
[26] Malla A, Dar F and Shah M 2017 *Current Nanomaterials* **2** 39–44
[27] Lee H, Kim K-H, Choi W H, Moon B C, Kong H J and Kang J K 2019 *ACS Appl. Mater. Interfaces* **11** 44366–74
[28] Nyarige J S, Krüger T P and Diale M 2020 *Materials Today Communications* **25** 101459
[29] Kyesmen P I, Nombona N and Diale M 2020 *Mater. Res. Bull.* **131** 110964
[30] Ling Y, Wang G, Reddy J, Wang C, Zhang J Z and Li Y 2012 *Angew. Chem.* **124** 4150–5
[31] Cui X, Liu T, Zhang Z, Wang L, Zuo S and Zhu W 2014 *Powder Technol.* **266** 113–9
[32] Lee H, Kim K-H, Choi W H, Moon B C, Kong H J and Kang J K 2019 *ACS Appl. Mater. Interfaces* **11** 44366–74
[33] De Faria D L, Venâncio Silva S and De Oliveira M 1997 *J. Raman Spectrosc.* **28** 873–8
[34] Jones R R, Hooper D C, Zhang L, Wolverson D and Valev V K 2019 *Nanoscale Res. Lett.* **14** 1–34
[35] Singh A P, Tossi C, Tittonen I, Hellman A and Wickman B 2020 *RSC Adv.* **10** 33307–16
[36] Saremi-Yarahmadi S, Wijayantha K U, Tahir A A and Vaidhyanathan B 2009 *The Journal of Physical Chemistry C* **113** 4768–78
[37] Wang J, White W B and Adair J H 2005 *J. Am. Ceram. Soc.* **88** 3449–54
[38] Jeon T H, Moon G.-h., Park H and Choi W 2017 *Nano Energy* **39** 211–8
[39] Shinde P S, Lee S Y, Choi S H, Lee H H, Ryu J and Jang J S 2016 *Sci. Rep.* **6** 1–14
[40] Li Q 2015 *The Study of Semiconductor Heterostructures for Photocatalysis and Photoelectrochemical Water Splitting* (Hong Kong: The Chinese University of Hong Kong)
[41] Oldham K B and Parnis J M 2017 *ChemTexts* **3** 5
[42] Huang M-C, Wang T, Wu C-C, Chang W-S, Lin J-C and Yen T-H 2014 *Ceram. Int.* **40** 10537–44
[43] Huang M-C, Wang T, Wu C-C, Chang W-S, Lin J-C and Yen T-H 2014 *Ceram. Int.* **40** 10537–44
[44] Li S, Cai J, Mei Y, Ren Y and Qin G 2014 *Int. J. Photoenergy* **2014** 794370
[45] Souza F L, Lopes K P, Nascente P A and Leite E R 2009 *Sol. Energy Mater. Sol. Cells* **93** 362–8
[46] Kong H, Jung J, Hwang S, Park J, Kim D H and Yeo J 2020 *J. Phys. Chem. Solids* **144** 109504
[47] Morrish R, Rahman M, MacElroy J and Wolden C A 2011 *ChemSusChem* **4** 474–9
[48] Poornajar M, Nguyen N T, Ahn H-J, Büchler M, Liu N, Kment S, Zboril R, Yoo J E and Schmuki P 2019 *Surfaces* **2** 131–44
[49] Landolsi Z, Assaker I B, Chtourou R and Ammar S 2018 *J. Mater. Sci., Mater. Electron.* **29** 8176–87
[50] Vanags M, Šutka A, Kleperis J and Shipkovs P 2015 *Ceram. Int.* **41** 9024–9
[51] Eunsoo Kim S K, moon Choi Y, Hyeok Park J and Shin H 2020 *ACS Sustainable Chem. Eng.* **8** 11358–67